

Yohannes S.M. Simamora^{1,2,*}, Harijono A. Tjokronegoro¹, Edi Leksono¹ & Irsan S. Brodjonegoro²

 ¹Engineering Physics Research Group, Institut Teknologi Bandung, Jalan Ganesa 10, Bandung 40132, Indonesia
 ²Department of Mechanical Engineering, Politeknik Purbaya, Jalan Pancakarya No. 1 Talang, Kabupaten Tegal 52193, Indonesia
 ³Offshore Engineering Research Group, Institut Teknologi Bandung, Jalan Ganesa 10, Bandung 40132, Indonesia
 *E-mail: ysmsimamora@yahoo.com

Highlights:

- Implementation of discrete raytracing approach to address a non-LoS ToF problem in LBL navigation.
- Estimation of Snell's parameter through a root-finding algorithm.
- Horizontal range computation using the estimated Snell's parameter.

Abstract. This paper presents an autonomous underwater vehicle (AUV) navigation scheme that pairs an inertial navigation system (INS) and a long baseline (LBL) acoustic positioning system. The INS is assigned to be the main navigation aid because of its faster rate. Meanwhile, the LBL provides position reference for compensation of the INS' main inherent drawback, i.e., accumulating errors. However, the LBL has to deal with time-of-flight (ToF) measurements that may not be carried out under line-of-sight (LoS) circumstances. This is because the propagation speed of underwater acoustic waves is subject to the sound-speedprofile (SSP) of the area in question. This paper's contribution is to consider the SSP in ToFs while addressing the above scheme. Specifically, the discrete approach to raytracing was implemented. For a given ToF, the Snell's parameter of the wave is estimated and subsequently used to compute the horizontal range. The ToF results are then used to estimate the xy position of the AUV, while the z position is obtained from a depth sensor. It was shown by simulation that the estimators can provide navigation with accuracy <0.5 m², as it manages to compensate for errors. Since the estimation of Snell's parameter is prone to exhibit imaginary numbers, future work should consider a more robust method to tackle this problem.

Keywords: long baseline; sensor fusion; sonar; sound speed profile; time-of-flight; underwater acoustics.

1 Introduction

Pairing an inertial navigation system (INS) with a reference system is necessary to maintain navigation accuracy. This prerequisite stems from INS' inherent tendency to accumulate errors over time [1]. In terrestrial and aerial applications, references are commonly provided by the global positioning system (GPS) [2]. This convenient system provides the position of a navigation subject based on the time-of-flight (ToF) measurement principle [3, p. 3]. However, GPS is virtually unavailable for autonomous underwater vehicle (AUV) navigation. This is due to the rapid attenuation of electromagnetic waves in water [4]. On the other hand, it was shown in [5] that underwater acoustic waves are less prone to attenuation and can travel at a range of hundreds of kilometers. Therefore, utilizing an acoustic positioning system instead for the aforementioned scheme for underwater settings is reasonable.

Among acoustic positioning systems, the long baseline (LBL) system is arguably the most suitable replacement for GPS. Aside of its resemblance to GPS in terms of configuration and measurement principle, LBL offers high accuracy, observation redundancy, and a larger operating area [6]. However, LBL is inherently subject to issues related to underwater acoustic propagation, e.g., multipath and bending trajectories [7]. Introducing any of these uncertainties to a ToF measurement rescinds the line-of-sight (LoS) assumption, i.e., the trajectory in question is a straight line. Thus, the ToF would result in a biased range, i.e., a pseudorange. Since LBL computes the position based on several ToFs, the presence of these biases will deteriorate the navigation accuracy. Multipath trajectories are also a problem in GPS [8], but bending trajectories are mostly related to underwater applications. For this reason, it is sensible to focus more on the latter issue when discussing LBL. Under the guidance of Snell's law, the propagation trajectory of a wave, the raytrace, will bend as its speed changes. On the other hand, the propagation speed of an underwater acoustic wave may vary during a ToF since it is a function of depth, salinity, and temperature [9]. Accordingly, its profile, known as the sound speed profile (SSP), is mostly unique for an area. In the literature (e.g., see [10]), the SSP is often represented as a curve of depth plotted against propagation speed.

There has been notable interest from researchers in navigation to consider bending raytrace (and the SSP as their root cause). In [11], possible positions of a node were estimated by plotting the raytrace with a constant range interval. Furthermore, bending raytrace in a ToF measurement are discussed in [12] by approximating the SSP as an isogradient function, i.e., a linear function of depth. This approach also inspired more recent works [13-15], which investigated localization accuracy. While an isogradient approach is suitable for capturing the

SSP in deep seas (e.g. see [16, p. 5]), it could be argued that to capture the SSP in shallower seas (e.g. see [17, p. 6]) requires a higher polynomial approximation.

On the other hand, different tightly coupled schemes for INS/LBL navigation have been reported in the literature. In a tightly coupled scheme, both sensor systems share a common filter [18, p. 251]. Its result provides an integrated navigation solution. This scheme offers more accuracy and robustness, as both systems complement each other. In [19], velocity and acceleration provided by an INS were included in the LBL state formulation. Other tightly coupled INS/LBL schemes are reported in [20, 21], where other sensors, i.e. Doppler velocity log (DVL) and magnetic compass pilot (MCP), were also included. It is worth noting that in all aforementioned approaches, the underwater sound speed was considered as a constant.

This paper presents an INS/LBL scheme for AUV navigation. Its main contribution is to address ToF measurements and LBL positioning when the actual SSP is approximated with a polynomial function. It departs from the existing schemes by also considering uncertainty due to the bending trajectory of acoustic waves. As an extension to our previous works [22, 23], the formulation of SSP, ToF, and pseudorange are now stated in general form. Furthermore, the single pseudorange approach was applied to an LBL system with *L* transponders. In the loosely coupled INS/LBL scheme, the position provided by the LBL is used as reference for error compensation in the INS. On the other hand, the INS compensation algorithm in [23] was expanded to errors exhibited in the accelerometer triad. The loosely coupled scheme was chosen for its simple implementation while still being considered sufficiently robust [18, p. 250].

2 Problem Statement

An AUV was deployed to follow a predefined trajectory in a shallow sea. The trajectory was in reach of an LBL system formed by L acoustic transponders with known and fixed positions, i.e., $\mathbf{r}_{o1} = \begin{bmatrix} x_{o1} & y_{o1} & z_{o1} \end{bmatrix}^T$,..., $\mathbf{r}_{oL} = \begin{bmatrix} x_{oL} & y_{oL} & z_{oL} \end{bmatrix}^T$. To accomplish the aforementioned task, the AUV was equipped with an INS, acoustic hydrophone arrays as the LBL receiver, and a depth sensor. These sensors were integrated in a loosely coupled scheme [18, p. 250], as shown in Figure 1. The inertial measurement units (IMU) in the INS consisted of accelerometer and gyroscope triads as the sensors. The dynamics of the LBL and INS subsystems are both described in discrete form, represented by sequences j and k, respectively, with sampling periods τ_{lbl} and τ_{lms} , respectively. At time t, the relationship between by j and k can be stated as:

$$k = f_{upd} \cdot j \,, \tag{1}$$

where $f_{upd} \coloneqq \frac{\tau_{lbl}}{\tau_{ins}}$. Since it is typical that $\tau_{lbl} > \tau_{ins}$, Eq. (1) implies that the position reference from the LBL is only available to the INS at each $f_{upd} \cdot j$ sequence, as shown in Figure 2.

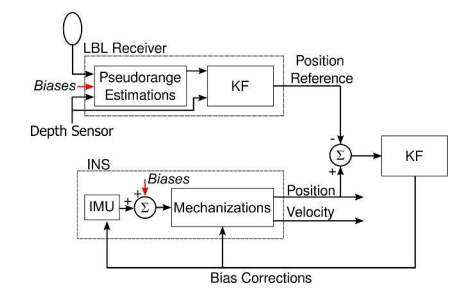


Figure 1 Loosely coupled scheme for INS/LBL integration.

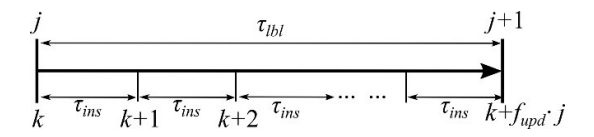


Figure 2 Evolution of the LBL and INS sequences within one time frame.

At the j^{th} sequence, the AUV at position $\mathbf{r}(j) = \begin{bmatrix} x(j) & y(j) & z(j) \end{bmatrix}^T$ engages in a ToF measurement with transponder l(l=1,...,L). Here, transponder l transmits an underwater acoustic wave at angle $\theta_{ol}(j)$, which will be received by the AUV at angle $\theta_{l}(j)$, as illustrated in Figure 3. The SSP in the area can be approximated with an S^{th} order polynomial function of depth, i.e.:

$$c(z) = \sum_{s=0}^{S} b_s z^s , (2)$$

where c(z) denotes the speed of sound at depth z, while b_s denotes depth of the s^{th} term of the polynomial, respectively. On the other hand, the wave propagates under the guidance of Snell's law [24], i.e.:

$$\frac{\cos \theta_{ol}(j)}{c(z_{ol})} = \dots = \frac{\cos \theta_{l}(j)}{c(z_{l}(j))} = \xi_{l}(j), \text{ and } \theta \in \left[-\frac{\pi}{2}, \frac{\pi}{2}\right], \tag{3}$$

where $\xi_i(j)$ denotes its respective Snell's parameters. If (2) is considered, the raytrace will bend during propagation to maintain a constant ratio in Eq. (3). As a result, the raytrace length, $s_i(j)$, may differ from the range, $d_i(j)$. When this is the case, the LoS assumption does not hold in the ToF.

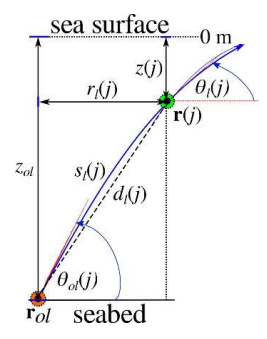


Figure 3 ToF measurement between the LBL's transponder and the AUV.

The above scenario is based on several assumptions. Firstly, the inertial frame coincides with the body frame. Second, the placement of the hydrophones and depth sensor represents the AUV's position in a local frame. Thirdly, the transponder's identity and transmission time stamp are encoded into every transmitted acoustic wave [25]. Fourthly, the AUV is set to achieve deployment while maintaining constant pitch and roll and a small yaw rate (\leq 5°/s). Accordingly, errors in the gyroscope triad during the course are less considered.

2.1 Biases in ToF Measurements

The dynamics of time-of-flight (ToF) measurement in the presence of biases for LBL navigation have been detailed in our previous work [26]. Hence, this subsection is written mostly as segue to the elaboration of pseudorange measurements in a polynomial SSP. Nonetheless, some departures in this paper are worth mentioning. Firstly, since information about z(j) can be obtained from the depth sensor, the ToF measurements will now be carried out only to provide a horizontal position reference, i.e., on the xy axes. Secondly, Eq. (2) is now introduced to the dynamics to replace a constant sound speed.

In the presence of a clock offset, the ToF measurement between the AUV and transponder *l* can be written as:

$$\Delta_{l}(j) = \delta_{l}(j) - \delta_{0}(j) + \phi(j), \tag{4}$$

where $\Delta_l(j)$ denotes the ToF, $\delta_0(j)$ and $\delta_l(j)$ are the transmission and reception time stamps of the acoustic wave, respectively, and $\phi(j)$ represents the offset of transponder l's clock toward the AUV's clock. Here, both $\delta_0(j)$ and $\phi(j)$ are assumed to be identical for all transponders. On the other hand, the dynamics of $\phi(j)$ can be written as [27]:

$$\phi(j+1) = \phi(j) + \tau_{clock}\alpha(j) + w(j), \tag{5}$$

where $\alpha(j)$ and τ_{clock} denote the clock skew and the offset sampling period, respectively, while w(j) is Gaussian noise. In [28], $\alpha(j)$ is modeled as P^{th} order autoregressive filter, i.e.

$$\alpha(p) = \sum_{p=1}^{p} a_{p} \alpha(p-1) + \eta(p),$$
 (6)

where a_p denotes the p^{th} coefficient that will be estimated as \hat{a}_p while $\eta(p)$ denotes Gaussian additive noise. By first defining $\mathbf{r}_{hor}(j) \coloneqq \begin{bmatrix} x(j) & x(j) \end{bmatrix}^T$ and $\mathbf{t}_l \coloneqq \begin{bmatrix} x_l & y_l \end{bmatrix}^T$, pseudorange measurement can then be stated as:

$$r_{l}(j) = \left\| \mathbf{r}_{hor}(j) - \mathbf{t}_{l} \right\| + c(z(j))\phi(j) + \rho_{l}(j), \tag{7}$$

where $r_l(j)$ denotes the horizontal pseudorange between the AUV and transponder l, c(z(j)) is the term of (1) for z(j), and $\rho_l(j)$ denotes the range uncertainty due to the motion of the AUV during the measurement.

2.2 Raytracing

In [29, p. 578], $\Delta_l(j)$ and $r_l(j)$ are computed incrementally as the wave in question travels from z_{ol} to z(j). To follow this approach, the vertical range between z_{ol} and z(j) is divided into N layers with identical thickness, $\zeta_l(j)$, as shown in Figure 4. This can be expressed as:

$$\zeta_{l}(j) = \frac{z_{ol} - z_{j}(j)}{N}.$$
(8)

Accordingly, it follows that

$$z_{ol} - z_{l(1)}(j) = z_{l(1)}(j) - z_{l(2)}(j) = \dots = z_{l(N-1)}(j) - z_{l(N)} = \zeta_l(k),$$

where $z_{l(n)}(j)$ (n=1,...,N) is the depth of the n^{th} layer, while $z_{0l} \equiv z_{l0}(j)$ and $z_{l(N)} \equiv z(j)$. Noticing that $z_{0l} > z(j)$, the vertical range can be stated as:

$$z(j) = z_{ol} - \sum_{n=1}^{N} z_{l(n)}(j).$$

$$z_{l(N-I)}(j)$$

$$z_{l(N)}(j) = z(j)$$

Figure 4 Vertical range divided into layers with identical thickness.

For a given z(j) in Eq. (9), the incremental traveling time and horizontal range equations in [29] can now be stated as:

$$\Delta_{l}(j) = \sum_{n=1}^{N} \left\{ \frac{1}{\frac{d}{dz} c(z_{l(n-1)}(j))} \ln \left[\frac{c(z_{l(n)}(j))}{c(z_{l(n-1)}(j))} \right] \right\}, \tag{10}$$

$$\times \frac{1 + (1 - \xi_{l}^{2}(j)c^{2}(z_{(n-1)l}(j)))^{\frac{1}{2}}}{1 + (1 - \xi_{l}^{2}(j)c^{2}(z_{l(n)}(j)))^{\frac{1}{2}}} \right\},$$

and:

$$r_{l}(j) = \sum_{n=1}^{N} \left\{ \frac{1}{\left[\frac{d}{dz}c(z_{(n-1)l}(j))\right]} \xi_{l}^{2}(k) \left[\left(1 - \xi_{m}^{2}(j)c^{2}(z_{l(n-1)}(j))\right)^{\frac{1}{2}} - \left(1 - \xi_{l}^{2}(j)c^{2}(z_{l(n-1)}(j))\right)^{\frac{1}{2}} \right] \right\}$$

$$(11)$$

respectively. It should be noted that Eqs. (10) and (11) apply for $\xi_l^2(j)c^2(z_{l(n-1)}(j))<1$, i.e., where the wave has not achieved its peak in Eq. (3).

Since $c(z_{l(n)}(j))$ can be computed at any depth using (1), $\xi_l(j)$ will be the only unknown parameter in Eqs. (10) and (11). This implies that if $\xi_l(j)$ can be obtained for a given $\Delta_l(j)$, then $r_l(j)$ can be also computed.

If $r_1(j),...,r_L(j)$ are available for $L \ge 3$ transponders [3, p. 163], measurement for $\mathbf{r}_{hor}(j)$ can be provided through a least squares solution [30, p. 219]:

$$\mathbf{r}_{hor}(j) = (\mathbf{t}^T \cdot \mathbf{t})^{-1} \cdot (\mathbf{t}^T \cdot \mathbf{\rho}(j)), \tag{12}$$

where:

$$\mathbf{t} = \left[\left(\mathbf{t}_1 - \mathbf{t}_2 \right)^T \quad \cdots \quad \left(\mathbf{t}_{L-1} - \mathbf{t}_L \right)^T \right]^T \in \square^{U \times 2},$$

and:

$$\rho(j) = \frac{1}{2} \begin{bmatrix} r_2^2(j) - r_1^2(j) + \mathbf{t}_1^T \cdot \mathbf{t}_1 - \mathbf{t}_2^T \cdot \mathbf{t}_2 \\ \vdots \\ r_L^2(j) - r_{L-1}^2(j) + \mathbf{t}_L^T \cdot \mathbf{t}_L - \mathbf{t}_{L-1}^T \cdot \mathbf{t}_{L-1} \end{bmatrix} \in \square^U,$$

where U = L(L-1)/2 are the possible combinations of pseudorange differences [31], i.e., $r_l(j) - r_m(j)$, (m = 1,...,L but $l \neq m$.).

2.3 LBL State Space Representation

To formulate a state space representation of the LBL, its state vector is specified as:

$$\mathbf{x}(j) := \begin{bmatrix} \mathbf{x}_{1}(j) \\ x_{2}(j) \\ \mathbf{x}_{3}(j) \\ x_{4}(j) \\ x_{5}(j) \\ x_{6}(j) \\ \vdots \\ x_{5+P}(j) \\ x_{6+P}(j) \\ \vdots \\ x_{6+P+U}(j) \end{bmatrix}$$

where $\mathbf{v}_{hor}(j)$ and $v_z(j)$ denote horizontal and vertical speed in a linear motion, while the AR filter in Eq. (6) is now stated in sequence j. The structure of the above state vector is very similar to the one defined in [26], except that z(i) and $v_{z}(i)$ are now excluded from the kinematics related to the ToF measurements. Accordingly, the state space representation of the LBL can now be stated as:

$$\mathbf{x}(j+1) = \mathbf{A}(k)\mathbf{x}(j) + \mathbf{w}(j)$$

$$\mathbf{y}(j+1) = \mathbf{C}\mathbf{x}(j+1) + \mathbf{d}(j+1)$$
(13)

where:

$$\mathbf{A}(j) = \begin{bmatrix} \mathbf{I}_{2\times 2} & 0 & \boldsymbol{\tau}_{lbl} \mathbf{I}_{2\times 2} & 0 & 0 & \mathbf{0}_{2\times P} & \mathbf{0}_{2\times U} \\ \mathbf{0}_{1\times 2} & 1 & \mathbf{0}_{1\times 2} & \boldsymbol{\tau}_{lbl} & 0 & \mathbf{0}_{1\times P} & \mathbf{0}_{1\times U} \\ \mathbf{0}_{2\times 2} & 0 & \mathbf{I}_{2\times 2} & 0 & 0 & \mathbf{0}_{2\times P} & \mathbf{0}_{2\times U} \\ \mathbf{0}_{1\times 2} & 0 & \mathbf{0}_{1\times 2} & 1 & 0 & \mathbf{0}_{1\times P} & \mathbf{0}_{1\times U} \\ \mathbf{0}_{1\times 2} & 0 & \mathbf{0}_{1\times 2} & 0 & 1 & \mathbf{A}_{56} & \mathbf{0}_{1\times U} \\ \mathbf{0}_{P\times 2} & \mathbf{0}_{P\times 1} & \mathbf{0}_{P\times 2} & \mathbf{0}_{P\times 1} & \mathbf{0}_{P\times 1} & \mathbf{A}_{66} & \mathbf{0}_{P\times U} \\ \mathbf{0}_{U\times 2} & \mathbf{0}_{U\times 1} & \mathbf{A}_{73}(j) & \mathbf{0}_{U\times 1} & \mathbf{A}_{75}(j) & \mathbf{A}_{76}(j) & \mathbf{A}_{77}(j) \end{bmatrix},$$

consisting of the following sub matrices:

$$\mathbf{A}_{56} = \begin{bmatrix} \tau_{clock} & 0 & \dots & 0 \end{bmatrix} \in \Box^{1\times P}, \mathbf{A}_{66} = \begin{bmatrix} \hat{a}_{1} & \hat{a}_{2} & \dots & \hat{a}_{P-1} & \hat{a}_{P} \\ 1 & 0 & \dots & 0 & 0 \\ 0 & 1 & \dots & 0 & 0 \\ \dots & \dots & \dots & \dots \\ 0 & 0 & \dots & 1 & 0 \end{bmatrix} \in \Box^{P\times P},$$

$$\mathbf{A}_{73}(j) = 2\tau_{lbl} \begin{bmatrix} (\mathbf{t}_{1} - \mathbf{t}_{2})^{T} \\ r_{1}(j+1) + r_{2}(j+1) \end{bmatrix} \cdots \frac{(\mathbf{t}_{L-1} - \mathbf{t}_{L-2})^{T}}{r_{L-1}(j+1) + r_{L}(j+1)} \end{bmatrix}^{T} \in \Box^{U\times 2},$$

$$\mathbf{A}_{73}(j) = 2\tau_{lbl} \left[\frac{(\mathbf{t}_{1} - \mathbf{t}_{2})^{T}}{r_{1}(j+1) + r_{2}(j+1)} \quad \cdots \quad \frac{(\mathbf{t}_{L-1} - \mathbf{t}_{L-2})^{T}}{r_{L-1}(j+1) + r_{L}(j+1)} \right]^{T} \in \square^{U \times 2},$$

$$\mathbf{A}_{75}(j) = 2c(z(j)) \begin{bmatrix} \frac{[r_{1}(j+1) - r_{2}(j+1)] - [r_{1}(j) - r_{2}(j)]}{r_{1}(j+1) + r_{2}(j+1)} \\ \vdots \\ \frac{[r_{L-1}(j+1) - r_{L}(k+1)] - [r_{L-1}(j) - r_{L}(j)]}{r_{L-1}(j+1) + r_{L}(j+1)} \end{bmatrix} \in \square^{U},$$

$$\mathbf{A}_{76}(j) = 2c(z(j))\tau_{clock}\begin{bmatrix} \frac{[r_{1}(j+1)-r_{2}(j+1)]-[r_{1}(j)-r_{2}(j)]}{r_{1}(j+1)+r_{2}(j+1)} & 0 & \dots & 0\\ \vdots & & & 0 & \dots & 0\\ \frac{[r_{L-1}(j+1)-r_{L}(j+1)]-[r_{L-1}(j)-r_{L}(j)]}{r_{L-1}(j+1)+r_{L}(j+1)} & 0 & \dots & 0 \end{bmatrix}$$

$$\in^{U\times P}$$

and

$$\mathbf{A}_{77}(j) = \operatorname{diag}\left(\frac{r_1(j) - r_2(j)}{r_1(j+1) + r_2(j+1)}, \dots, \frac{r_{L-1}(j) - r_L(j)}{r_{L-1}(j+1) + r_L(j+1)}\right) \in \square^{U \times U};$$

 $\mathbf{w}(j) \in \square^{2+l+2+l+l+P+U}$ and $\mathbf{d}(j) \in \square^{2+l+U}$ denote process and measurement noise vectors, respectively, and

$$\mathbf{C} = \begin{bmatrix} \mathbf{I}_{2\times 2} & 0 & \mathbf{0}_{2\times 2} & 0 & 0 & \mathbf{0}_{2\times P} & \mathbf{0}_{2\times U} \\ \mathbf{0}_{1\times 2} & 1 & \mathbf{0}_{1\times 2} & 0 & 0 & \mathbf{0}_{1\times P} & \mathbf{0}_{1\times U} \\ \mathbf{0}_{U\times 2} & \mathbf{0}_{U\times 1} & \mathbf{0}_{U\times 2} & \mathbf{0}_{U\times 1} & \mathbf{0}_{U\times 1} & \mathbf{0}_{U\times P} & \mathbf{I}_{U\times U} \end{bmatrix}.$$

2.4 Errors in the IMU

To represent errors in the IMU [32], the measurement biases in the accelerometer triad are represented here by:

$$\mathbf{\varepsilon}_{f}^{b}(k) \coloneqq \begin{bmatrix} \mathbf{\varepsilon}_{f(cs)}^{b}(k) & \mathbf{\varepsilon}_{f(rv)}^{b}(k) & \mathbf{\varepsilon}_{f(gp)}^{b}(k) \end{bmatrix}^{T} \in \Box^{3+3+3},$$

where $\mathbf{\epsilon}_{f(cs)}^{b}(k)$, $\mathbf{\epsilon}_{f(rw)}^{b}(k)$, $\mathbf{\epsilon}_{f(gp)}^{b}(k)$ denote the constant, random-walk, and first-order Gauss-Markov (GM) process biases, respectively. Their dynamics can be stated as:

$$\mathbf{\varepsilon}_{f}^{b}\left(k+1\right) = \mathbf{F}_{f}\mathbf{\varepsilon}_{f}\left(k\right) + \mathbf{w}_{j}^{b}\left(k\right) \tag{14}$$

where:

$$\mathbf{F}_{f} = \begin{bmatrix} \mathbf{I} & \mathbf{0} & \mathbf{0} \\ \mathbf{0} & \mathbf{I} & \mathbf{0} \\ \mathbf{0} & \mathbf{0} & -\boldsymbol{\beta}_{f(gp)} \end{bmatrix} \in \Box^{(3+3+3)\times(3+3+3)} ,$$

while $\beta_f = \operatorname{diag}(\beta_{f_{ib}}, \beta_{f_{jb}}, \beta_{f_{jb}}) \in \square^{3\times3}$ represents the GM process parameters associated with the accelerometer triad and

$$\mathbf{w}_f^b(k) = \begin{bmatrix} \mathbf{0} & \mathbf{w}_{f(nv)}^b(k) & \mathbf{w}_{f(sp)}^b(k) \end{bmatrix}^T \in \square^{3+3+3},$$

denotes the noise vector of the accelerometer errors, where $\mathbf{w}^b_{f(re)}(k)$ and $\mathbf{w}^b_{f(ge)}(k)$ represent random walk and Gauss-Markov process noise, respectively. Here,

$$\mathbf{w}_{f(ro)}^{b}(k+1) = \mathbf{w}_{f(ro)}^{b}(k) + \tau_{ins}\mathbf{\eta}_{f(rw)}^{b}(k),$$

where $\eta_{\text{final}}^{b}(k)$ is the vector of its related Gaussian noise. Furthermore,

$$\mathbf{w}_{f(gp)}^{b}(k) = \left[\sqrt{2\beta_{fxb}\sigma_{fxb}^{2}} \quad \sqrt{2\beta_{fyb}\sigma_{fyb}^{2}} \quad \sqrt{2\beta_{fzb}\sigma_{fzb}^{2}} \right] \mathbf{\eta}_{f(gp)}^{b}(k),$$

where σ_{fxb} , σ_{fxb} , σ_{fbz} are variances associated with the accelerometer errors, while $\eta_{f(gp)}^{b}$ is a 3×1 vector of additional noise in the GM process.

To formulate a state-space representation of INS errors in a local frame, it is defined that $\mathbf{\varepsilon}(k) \coloneqq \begin{bmatrix} \mathbf{\varepsilon}_p(k) & \mathbf{\varepsilon}_v(k) & \mathbf{\varepsilon}_f(k) \end{bmatrix}^T \in \Box^{3+3+9}$, where $\mathbf{\varepsilon}_p(k)$ and $\mathbf{\varepsilon}_v(k)$ denote the position and velocity errors in the local frame, respectively. Subsequently, the vector of the respective process noises is stated as:

$$\mathbf{w}(k)\!\coloneqq\!\!\begin{bmatrix}\mathbf{0} & \mathbf{0} & \mathbf{0} & \mathbf{w}_{f(nv)}^{b}(k) & \mathbf{w}_{f(gp)}^{b}(k)\end{bmatrix}^{T}\!\in\!\Box^{3+3+3+3}\;.$$

It can then be written that:

$$\begin{cases} \mathbf{\varepsilon}(k+1) = \mathbf{F}\mathbf{\varepsilon}(k) + \mathbf{w}(k) \\ \mathbf{y}_{\varepsilon}(k+1) = \mathbf{G}\mathbf{\varepsilon}(k+1) + \mathbf{d}_{\varepsilon}(k+1) \end{cases}$$
(15)

where:

$$\mathbf{F} = \begin{bmatrix} \mathbf{I} & \tau_{ins} \mathbf{I} & \mathbf{0} \\ \mathbf{0} & \mathbf{I} & \tau_{ins} \mathbf{R}_b^{loc} \left(k \right) \\ \mathbf{0} & \mathbf{0} & \mathbf{F}_f \left(k \right) \end{bmatrix} \in \Box^{(3+3+9)\times(3+3+9)},$$

$$G = \begin{bmatrix} I & 0 & 0 \end{bmatrix} \in \Box^{3 \times (3+3+9)},$$

and:

$$\mathbf{R}_{b}^{loc}\left(k\right) = \begin{bmatrix} 1 & -\tau_{ins}\omega_{zb}\left(k\right) & \tau_{ins}\omega_{yb}\left(k\right) \\ \tau_{ins}\omega_{zb}\left(k\right) & 1 & -\tau_{ins}\omega_{xb}\left(k\right) \\ -\tau_{ins}\omega_{yb}\left(k\right) & \tau_{ins}\omega_{xb}\left(k\right) & 1 \end{bmatrix},$$

is a transformation matrix [18] that transforms the accelerations values from the body frame in the IMU to a local frame, while $\omega_{xb}(k)$, $\omega_{yb}(k)$, and $\omega_{zb}(k)$ are the three-dimensional angular speeds provided by the gyroscope triad.

2.5 INS Mechanization

To include the exhibited errors at the IMU to the INS mechanization, the acceleration is written as:

$$\mathbf{a}(k) = \mathbf{R}_{b}^{loc}(k) \left[\mathbf{f}_{ins}^{b}(k) + \mathbf{\varepsilon}_{f(cs)}^{b}(k) + \mathbf{\varepsilon}_{f(rw)}^{b}(k) + \mathbf{\varepsilon}_{f(rw)}^{b}(k) \right] + \overline{\mathbf{g}},$$
(16)

where $\mathbf{f}_{ins}^{b}(k)$ and $\overline{\mathbf{g}}$ denote specific forces and gravity, respectively. The INS mechanization can be defined as:

$$\mathbf{x}_{ins}(k) := \begin{bmatrix} \mathbf{r}_{ins}(k) & \mathbf{v}_{ins}(k) & \mathbf{a}_{ins}(k) \end{bmatrix}^T \in \square^{3+3+9}$$

where $\mathbf{r}_{ins}(k)$ and $\mathbf{v}_{ins}(k)$ denote the position and the velocity provided by the INS. Its dynamics can be stated as:

$$\mathbf{x}_{ins}(k+1) = \mathbf{A}_{ins}(k)\mathbf{x}_{ins}(k), \tag{17}$$

where:

$$\mathbf{A}_{ins}(k) = \begin{bmatrix} \mathbf{I} & \tau_{ins}\mathbf{I} & \mathbf{0} \\ \mathbf{0} & \mathbf{I} & \tau_{ins}\mathbf{I} \\ \mathbf{0} & \mathbf{0} & \mathbf{I} \end{bmatrix} \in \Box^{(3+3+9)\times(3+3+9)}.$$

2.6 Compensation Mechanism

In a loosely coupled scheme [26], interaction between the INS and its references, i.e., LBL and the depth sensors can be written as:

$$\mathbf{\varepsilon}_{P}(k) = \begin{bmatrix} \mathbf{x}_{1}(j) & x_{2}(j) \end{bmatrix}^{T} - \mathbf{r}_{ins}(k), \tag{18}$$

which will hold when $k = f_{upd} \cdot j$. This implies that compensation using Eq. (15) can be carried out only if Eq. (13) is available. When this is the case, $\mathbf{r}_{ins}(k)$ and $\mathbf{v}_{ins}(k)$ in Eq. (17) will be calculated using compensated values fed by Eq. (16).

3 Proposed Solution

It can be seen that solving Eq. (10) is a root-finding problem, i.e. to estimate $\xi_l(j)$ such that the function $h(\xi_l(j)) = 0$, where:

$$h(\xi_{l}(j)) := \sum_{n=1}^{N} \left\{ \left| \frac{1}{\frac{d}{dz} c(z_{l(n-1)}(j))} \right| \ln \left[\frac{c(z_{l(n)}(j))}{c(z_{l(n-1)}(j))} \right] \right\},$$

$$\times \frac{1 + \left(1 - \xi_{l}^{2}(j) c^{2}(z_{(n-1)l}(j))\right)^{\frac{1}{2}}}{1 + \left(1 - \xi_{l}^{2}(j) c^{2}(z_{l(n)}(j))\right)^{\frac{1}{2}}} \right\} - \Delta_{l}(j)$$
(19)

i.e., the subtraction of the right side of Eq. (10) with the left one. To solve Eq. (19) for $h(\xi_i(j)) = 0$, a standard regula falsi method [33] can be implemented. This method is chosen because it guarantees estimation convergence [34, p. 122]. A regula falsi flowchart for Eq. (19) is shown in Figure 5. Specifically, the lower and upper initial guesses are computed using the Snell equation in Eq. (3). On the other hand, $c(z_{ol})$ can be computed using the SSP equation in (2). It should also be noted that i represents the ith iteration of the algorithm.

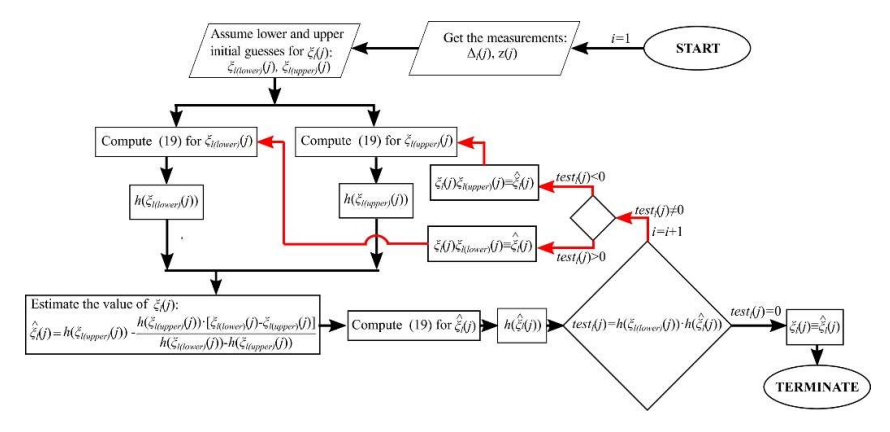


Figure 5 Regula falsi flow diagram for $\xi_i(j)$ estimation.

Meanwhile, it can be seen that both Eqs. (13) and (15) are linear systems with Gaussian noise. Therefore, a standard Kalman filter [35] was chosen as the estimator for both systems.

To recap, a diagram block of the proposed loosely coupled INS/LBL scheme is shown in Figure 6. It can be seen that the INS modeled errors in Eq. (15) exhibit uncertainties in the $\mathbf{f}_{\text{ins}}^b(k)$ measurements. Therefore, it may be necessary to add error compensation to the scheme besides the correction routine. Meanwhile, it should be noted that $\mathbf{\omega}_b(k)$, i.e., the outputs of the gyroscope triad, are fed to \mathbf{T} and to the modeled errors in the form of $\mathbf{R}_b^{loc}(k)$.

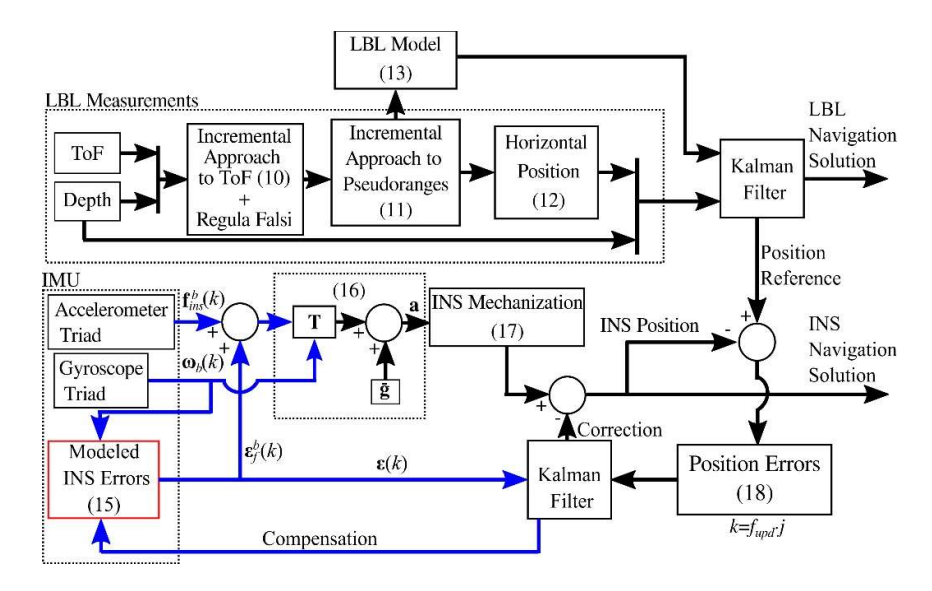


Figure 6 Block diagram of the proposed loosely coupled INS/LBL scheme.

4 Simulation

4.1 Numerical Setup

SSP – The actual SSP and Matlab code for polyfitting and raytracing were taken from [36]. Specifically, depth interval 45 < z < 68 m was chosen to represent the SSP's nonlinearity. Similar to [22], choosing S = 2 for Eq. (2) when curve fitting the actual SSP, gave $b_0 = 1529.78$, $b_1 = 0.352$ and $b_2 = -0.00628$ with an error percentage of 0.025%. It follows that $c(z) = 1529.78 + 0.352z - 0.00628z^2$

, while its derivative with respect to z in Eqs. (10) and (11) was dc(z)/dz = 0.352 - 0.01256z.

For the SSP's corresponding raytracing, acoustic transponder l was set to transmit waves with an aperture of 0° to 17.5° . Thus, solving Eq. (10) is essentially to find the unique value of $\theta_{ol}(j)$ from this aperture. Accordingly, the lower and upper initial guesses for the regula falsi algorithm were set to $\xi_{l}(j)$ = $\cos 17.5^{\circ}/c(68)$ and $\xi_{l}(j)=\cos 8^{\circ}/c(68)$, respectively. The algorithm is expected to provide a solution after seven iterations. On the other hand, N in Eq. (10) was set to 60, while in Eq. (11) N was set to 250.

The approximated SSP and its corresponding raytraces are shown in Figure 7. From the raytracing profile it can be seen that the ToF would not necessarily meet LoS condition. Furthermore, there is a shadow zone on the left side of the profile. This means that ToFs between transponder *l* and the AUV would not occur inside this particular region.

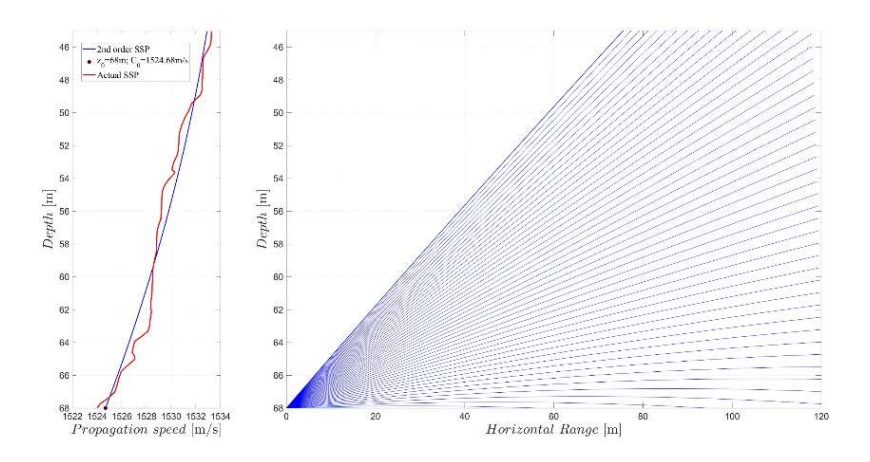


Figure 7 Second-order SSP and its corresponding raytracing.

LBL – The LBL is formed by four transponders (L=4), i.e., $\mathbf{r}_{o1} = \begin{bmatrix} 60 & 45 & 68 \end{bmatrix}^T$ m, $\mathbf{r}_{o2} = \begin{bmatrix} 20 & 175 & 68 \end{bmatrix}^T$ m, $\mathbf{r}_{o3} = \begin{bmatrix} 175 & 175 & 68 \end{bmatrix}^T$ m, and $\mathbf{r}_{o4} = \begin{bmatrix} 165 & 60 & 68 \end{bmatrix}^T$ m. It is considerably small, e.g., compared to the baseline setup in [19] (1000×1000 m²) or our previous work [26] (1600×1600 m²). This size constriction is a result of introducing the SSP to design considerations. By inspecting Figure 7, it can be seen that an acoustic ray would reach its peak around 120 m. It should be recalled

that tracing beyond a peak is excluded by the constraint in Eqs. (10)-(11). Moreover, the size of the operating region is also reduced by shadow zones inside the LBL. In a technical sense, installing more transponders may be a solution when an application requires a larger LBL. A more fundamental approach to this limitation would be to relax the aforementioned constraint.

Meanwhile, the AR filter in Eq. (6) was parameterized for P=5, where its estimated values, i.e., $[\hat{a}_1,...,\hat{a}_s]=[0.9271\ 0.4163\ 0.07843\ -0.387\ -0.03118]$ were taken from [28]. Furthermore, the initial values for clock offset and skew were set to $\phi(0)=0.03$ s and $\alpha(0)=3\cdot10^4$ s/s, respectively, and its period was set to $\tau_{clock}=10$ s.

INS – The update rate of the INS was set to 64 Hz, i.e., $\tau_{ms} = 0.015625$ s. The initial biases in the IMU were set to $\varepsilon_{f(cs)}^b(0) = \begin{bmatrix} 0.1 & 0.1 \end{bmatrix}^T \text{m/s}^2$, $\varepsilon_{f(rw)}^b(0) = \begin{bmatrix} 0 & 0 & 0 \end{bmatrix}^T \text{m/s}^2$, while the GM parameters were set to $\beta_f = \mathbf{I}_{3\times 3}$. Since the AUV was set to move with simple maneuvers, the gravity biases supposedly added to $\varepsilon_{f(cs)}^b$ were assumed to cancel each other out with $\overline{\mathbf{g}}$.

4.2 Simulation Scenario

The AUV was launched from START = $\begin{bmatrix} 125 & 125 & 51 \end{bmatrix}^T$ m and expected to reach FINISH = $\begin{bmatrix} 100.34 & 100.38 & 46.8 \end{bmatrix}^T$ m in 200 s, i.e., at j = 200 and k = 12,800. It would follow a helix shaped trajectory, as represented by the solid green line in Figure 6. During the given time, it was expected that the dynamics of the INS/LBL could be evaluated. On the other hand, the AUV would move in a circular motion in the horizontal plane (the xy axes) to follow the trajectory. This means that the gyroscope triad mentioned in Eqs. (15) and (16) would contribute to the navigation.

To achieve this objective, the AUV initial sway (pitch) and heave (yaw) were set to 11.26° and 5° , respectively, while its initial surge (roll) was not addressed, as its dynamic model is unknown. Nonetheless, the sway and surge would remain constant during deployment. The maneuvering of the AUV would then depend on a constant vertical and angular speed, which was set to -0.021 m/s and $\left[\omega_{xb}(k) \quad \omega_{yb}(k) \quad \omega_{zb}(k)\right] = \left[0 \quad 0 \quad 0.087\right] \text{ rad/s, respectively.}$

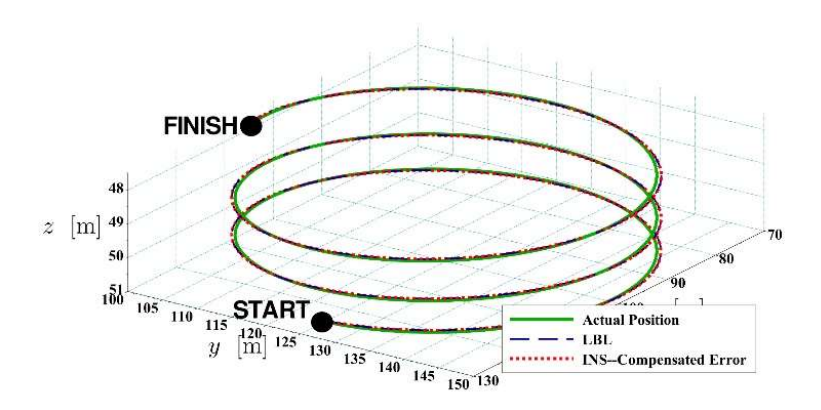


Figure 8 The AUV trajectory tracked by the LBL and INS estimators.

4.3 Results and Discussion

As shown in Figure 6, both estimators in the LBL and INS managed to closely track the AUV's trajectory. A closer inspection of the LBL errors from the AUV's actual position during the course is shown in Figure 9. In terms of the acoustic positioning system [6], the LBL provided good accuracy, as errors in each axis were less than 1 m or 1 m² on the horizontal axes.

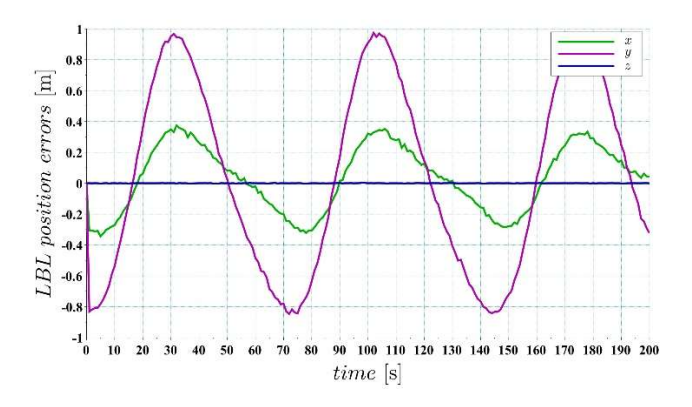


Figure 9 LBL errors from the AUV's actual position.

The INS errors from the AUV's position are shown in Figure 10. The similarity to the LBL errors in Figure 9 indicates that the estimator in the INS managed to compensate for the errors. This could be achieved even though corrections from the LBL were only available every $k = 64 \cdot j$. The INS errors from the actual velocity in Figure 11 also indicate this.

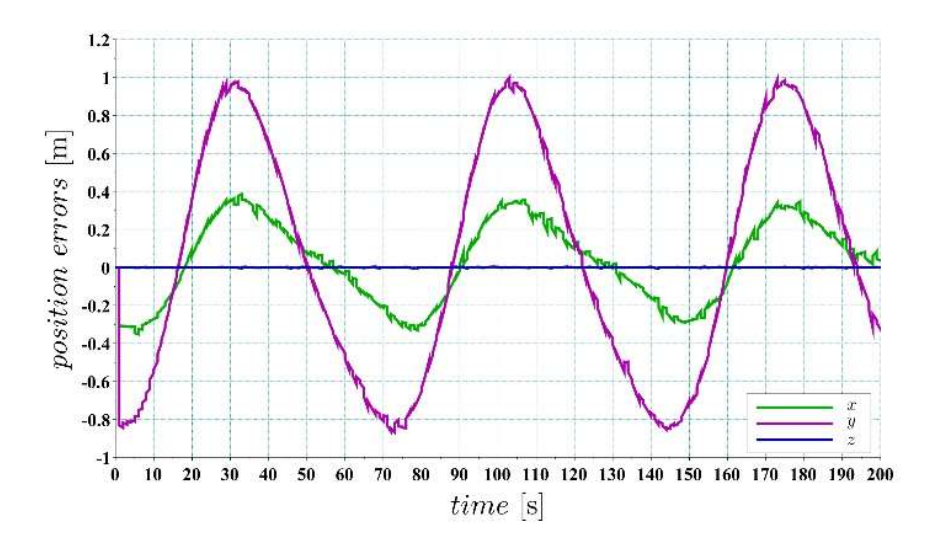


Figure 10 INS errors from the AUV's actual position.

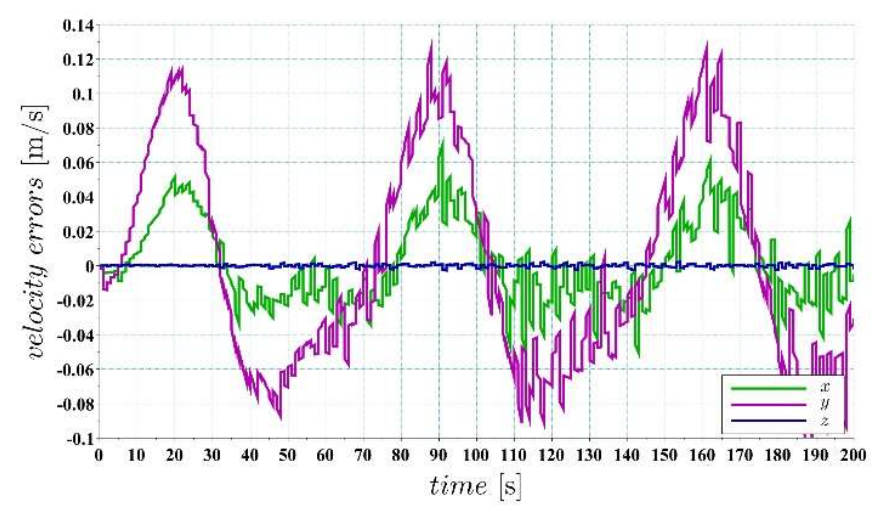


Figure 11 INS errors from the AUV's actual velocity.

As described in Figure 6, the proposed scheme also compensated errors at the IMU level. This is a departure from our previous work [23], which only dealt with correction in the INS mechanization. The compensation of these modeled errors is shown in Figure 12, i.e., constant, random walk, and Gauss-Markov errors, respectively.

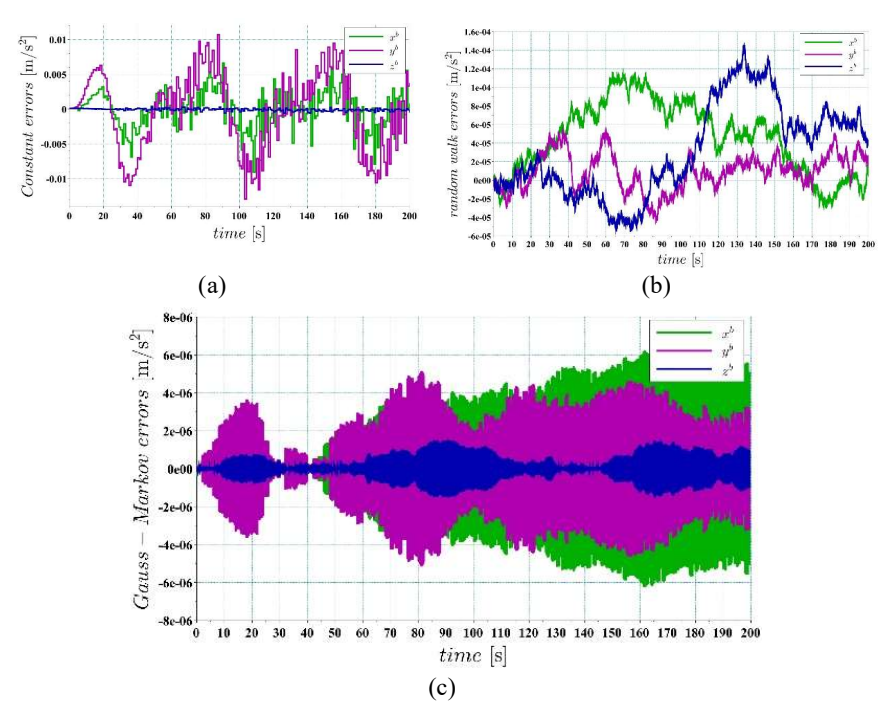


Figure 12 Error compensation at the accelerometer triad: (a) constant, (b) random walk, (c) Gauss-Markov.

The INS/LBL performance is indicated by the average standard of deviation, as shown in Table 1. Superscript (\sim) above a variable in Table 1 indicates that it is an estimated value. The values were obtained by repeating the above simulation more than 1,000 times. From deviations of $\tilde{\bf r}_{lbl}$ at the xy axes, it is shown that the LBL could provide navigation with horizontal accuracy less than 0.5 m². On the other hand, it was also shown that the deviations of the estimated positions in LBL and INS were very similar. Therefore, it can be argued that INS performance largely depends on the accuracy of the references provided by the LBL.

 Table 1
 INS/LBL estimation and compensation performance.

Estimated Variables	Average Standard of Deviation	
$ ilde{\mathbf{r}}_{lbl}$	$[0.21 \ 0.61 \ 97 \cdot 10^{-5}]^T$	m
$ ilde{f r}_{ins}$	$[0.21 \ 0.61 \ 51 \cdot 10^{-4}]^T$	m
$ ilde{ extbf{v}}_{ins}$	$[27 \cdot 10^{-3} 62 \cdot 10^{-3} 8 \cdot 10^{-3}]^T$	m/s
$ ilde{oldsymbol{arepsilon}}^b_{f(cs)}$	$[64 \cdot 10^{-4} \ 83 \cdot 10^{-4} \ 71 \cdot 10^{-4}]^T$	m/s^2
$\widetilde{m{arepsilon}}_{f(rw)}^{b}$	$[43 \cdot 10^{-4} \ 43 \cdot 10^{-4} \ 42 \cdot 10^{-4}]^T$	m/s^2
$\widetilde{\boldsymbol{\varepsilon}}^b_{f(gp)}$	$[98 \cdot 10^{-6} 10^{-4} 97 \cdot 10^{-6}]^T$	m/s^2

5 Conclusions

Compensation of errors in a loosely coupled INS/LBL navigation scheme was presented. The navigation scheme considers ToF measurements, where the wave propagation speed is subject to a polynomial SSP. For a given ToF, its Snell's parameter is estimated through an incremental approach and a root-finding algorithm. The same approach is also implemented to compute its corresponding pseudorange. At the INS, compensation is carried out at the IMU, while correction is applied to the mechanization. By simulation, it was shown that the LBL managed to provide a position reference to the INS with horizontal accuracy less than 0.5 m². Using the LBL reference, the INS managed to correct and compensate for errors and provided navigation with position accuracy close to the LBL references, i.e., $[0.21\ 0.61\ 51\cdot 10^{-4}]^T$ m.

Future works should consider scenarios that include drift in orientation due to gyroscope biases. On the other hand, a more robust root-finding method should be considered, as the estimation of Snell's parameter in Eq. (19) is prone to exhibit imaginary numbers. Moreover, the soundness of the proposed solution needs to be tested further through physical realization and experiments.

Acknowledgement

This work was sponsored by LPDP Indonesia under contract no. PRJ-5786/LPDP.3/2016.

References

- [1] Titterton, D., Weston, J.L. & Weston, J., Strapdown Inertial Navigation Technology, 17, IET, 2004.
- [2] Schmidt, G.T., *INS/GPS Technology Trends*, NATO RTO Report RTO-EN-SET-064, 2004.
- [3] Bensky, A., Wireless Positioning Technologies and Applications 2nd ed., Artech House, 2016.
- [4] Al-Shamma'a, A.I., Shaw, A. & Saman, S., *Propagation of Electromagnetic Waves at MHz Frequencies through Seawater*, IEEE Trans. Ant. Prop., **52**(11), pp. 2843-2849, 2004.
- [5] Thorp, W.H., Deep-Ocean Sound Attenuation in the Sub and Low-Kilocycle-per-Second Region. J. Acoust. Soc. America, **38**(4), pp. 648-654, 1965.
- [6] Vickery, K., Acoustic Positioning Systems, A Practical Overview of Current Systems, in: Proc. the 1998 Workshop on AUV, pp. 5-17, 1998

- [7] Stojanovic, M. & Preisig, J., *Underwater Acoustic Communication Channels: Propagation Models and Statistical Characterization*, IEEE Comm. Mag., **47**(1), pp. 84-89, 2009.
- [8] Breßler, J., Reisdorf, P., Obst, M. & Wanielik, G., *GNSS Positioning in Non-Line-of-Sight Context A Survey*, 2016 IEEE ITSC, Rio de Janeiro, pp. 1147-1154, 2016.
- [9] Mackenzie, K.V., *Nine-Term Equation for Sound Speed in the Oceans*, J. Acoust. Soc. America, **70**(3), pp. 807-812, 1981.
- [10] Etter, P.C., *Underwater Acoustic Modeling and Simulation 5th ed.* CRC Press, 2018.
- [11] Ameer, P.M. & Jacob, L., Localization Using Ray Tracing for Underwater Acoustic Sensor Networks, IEEE Comm. Lett., 14(10), 930-932, 2010
- [12] Ramezani, H., Jamali-Rad, H., & Leus, G., *Target Localization and Tracking for an Isogradient Sound Speed Profile*, IEEE Trans. Sign. Proc., **61**(6), pp. 1434-1446, 2013.
- [13] Zhang, Y., Li, Y., Zhang, Y. & Jiang, T., Underwater Anchor-AUV Localization Geometries with an Isogradient Sound Speed Profile: A CRLB-Based Optimality Analysis, IEEE Trans. Wireless Comm., 17(12), pp. 8228-8238, 2018.
- [14] Dong, Y., Sun, C. & Zhang, K., *Underwater Localization with Sound Velocity Profile*, Proc. 13th ACM Int. Conf. Underwater Netw. & Syst. ACM, Shenzen, China, 51, 2018.
- [15] Li, Y., Wang, W., Liu, M., Zhang, S. & Lian, J., *Underwater Target Tracking in Three-Dimensional Space Based on Sound Speed Profile*, Proc. 38th Chinese Contr. Conf., Ghuangzou, China, pp. 3052-3057, 2019.
- [16] Huang, C., Wu, M., Huang, X., Cao, J., He, J., Chen, C., Zhai, G., Deng, K. & Lu, X., Reconstruction and Evaluation of the Full-Depth Sound Speed Profile with World Ocean Atlas 2018 for the Hydrographic Surveying in the Deep-Sea Waters, App. Ocean Res., 101, pp. 1-12, 2020.
- [17] Wang, X., Khazaie, S. & Chen, X., Linear Approximation of Underwater Sound Speed Profile: Precision Analysis in Direct and Inverse Problems, App. Acoust., **140**, pp. 63-73, 2018.
- [18] Noureldin, A., Karamat, T.B. & Georgy, J., Fundamentals of Inertial Navigation, Satellite-based Positioning and Their Integration, Springer Science & Business Media, 2012.
- [19] Silva, T. & Batista, P., Long Baseline Navigation Filter with Clock-Offset Estimation, Nonlinear Dyn., 100, pp. 2557-2573, 2020.
- [20] Zhang, T., Shi, H., Chen, L., Li, Y., & Tong, J., AU Positioning Method Based on Tightly Coupled SINS/LBL for Underwater Acoustic Multipath Propagation. Sensors, 16(3), 357, 2016.
- [21] Zhang, T. Chen, L. & Li, Y., AUV Underwater Positioning Algorithm Based on Interactive Assistance of SINS and LBL, Sensors, 16(1), 42, 2016.

- [22] Simamora, Y.S.M., Brodjonegoro, I.S., Tjokronegoro, H.A. & Leksono, E., *On Pseudorange Estimation in a Quadratic Sound Speed Profile*, 2019 IEEE CSUDET, Penang, Malaysia, pp. 284-289, 2019.
- [23] Simamora, Y.SM., Tjokronegoro, H.A., Leksono, E. & Brodjonegoro, I.S., Compensation of INS Errors based on LBL References in a Quadratic Sound-Speed-Profile, ITIS, Surabaya, 2020.
- [24] Bahrami, N., Khamis, N.H.H., Baharom, A. & Yahya, A., *Underwater Channel Characterization to Design Wireless Sensor Network by Bellhop*. Telkomnika, **14**(1), pp. 110-118, 2016.
- [25] Webster, S.E., Eustice, R.M., Singh, H. & Whitcomb, L.L., *Advances in Single-Beacon One-Way-Travel-Time Acoustic Navigation for Underwater Vehicles*, Int. J. Robot. Res., **31**(8), pp. 935-949, 2012.
- [26] Simamora, Y.SM., Tjokronegoro, H.A., Leksono, E. & Brodjonegoro, I.S., Compensation of Time-Varying Clock-Offset in a LBL Navigation, BEEI, 9(4), pp. 1364-1372, 2020.
- [27] Kim, H.Y, *Modeling and Tracking Time-Varying Clock Drifts in Wireless Networks*, PhD diss., Georgia Institute of Technology, 2014.
- [28] Kim, H., Ma, X. & Hamilton, B.R., *Tracking Low-Precision Clocks with Time-Varying Drifts Using Kalman Filtering*. IEEE/ACM Trans. Netw., **20**(1), pp. 257-270, 2012.
- [29] Hovem, J.M., *Ray Trace Modeling of Underwater Sound Propagation*, Modeling and Measurement Methods for Acoustic Waves and for Acoustic Microdevices, IntechOpen, pp. 573-594, 2013.
- [30] Strang, G., *Introduction to Linear Algebra* 5th ed., Wellesley-Cambridge Press, 2016.
- [31] Batista, P., Long Baseline Navigation with Clock Offset Estimation and Discrete-Time Measurements, Contr. Eng. Pract., **35**, pp. 43-53, 2015.
- [32] Petritoli, E., Lecesse, F. & Leccisi, M., *Inertial Navigation Systems for UAV: Uncertainty and Error Measurements*, 2019 IEEE MetroAeroSpace, Torino, Italy, pp. 218-222, 2019.
- [33] Chen, J., New Modified Regula Falsi Method for Nonlinear Equations, App. Math. Comp., **184**(2), pp. 965-971, 2007.
- [34] Chapra, S.C., & Canale, R.P., *Numerical Methods for Engineers* 7th ed., McGraw-Hill, 2011.
- [35] Terajanu, G., *Discrete Kalman Filter Tutorial*, Dept. Computer Science and Engineering, University at Buffalo, 2013.
- [36] Brodjonegoro, I.S., Lecture on Advanced Underwater Acoustics, Ocean Engineering Graduate Program, ITB, January-April 2017.